ADVANCED MATERIALS TECHNOLOGIES
www.advmattechnol.de

Bimetallic MOF-Based Fibrous Device for Noninvasive Bilirubin Sensing

Zihan Lu, Zhijia Xiao, Jinlong Wang, Zhe Zhao, Jiayuan Huang, Jizhai Cui, Yongfeng Mei, and Gaoshan Huang**

Noninvasive and real-time detection of bilirubin concentration enables rapid assessment of liver health status and the diagnosis of jaundice-related diseases. Herein, the study proposes a strategy to uniformly grow bimetallic FeCo metal–organic framework (MOF) films onto the surface of carbonized electrospun nanofibers via a stepwise growth strategy involving an induction effect of oxide nanomembrane prepared by atomic layer deposition, to realize high-performance flexible nanofiber bilirubin sensors. Compared with monometallic MOF, the FeCo bimetallic MOF can attain a larger specific surface area, thus augmenting the exposed active sites. Furthermore, the synergistic interaction between the bimetallic active sites on the MOF film and the carbonized nanofibers enhances the electronic conduction network, thereby significantly enhancing the catalytic activity of the flexible electrode for bilirubin. The current nanofibers sensor exhibits excellent performance in bilirubin detection, in terms of high sensitivity, large linear detection range, and low detection limit. The synthesis of bimetallic MOF films on flexible fibers holds promise for the development of highly sensitive electrodes for wearable bilirubin detection devices.

1. Introduction

Bilirubin is a by-product of hemoglobin degradation.[1] In typical circumstances, the free bilirubin concentration in human serum is less than 25 μmol L^{-1}.[2] However, if the liver function is deficient, the body fails to get rid of free bilirubin adequately.[3] Under jaundice conditions, the levels can elevate to more than 50 μmol L^{-1}.[4] This excess of free bilirubin can pile up in different body organs, potentially leading to jaundice, brain damage, or even death.[5] Therefore, monitoring the free bilirubin concentration in human serum is worthy for diagnosing jaundice and liver disorders.[6] Previously, a variety of systematic methods have been developed for the quantitative measurement of bilirubin, such as direct spectroscopic and spectrofluorometric approaches.[7,8] However, these spectroscopic techniques can be influenced by interferences and azo-based reaction intermediates due to their pH sensitivity.[9] Other analytical detection methods, like polarography, and high-performance liquid chromatography, are also employed.[10,11] These methods tend to be expensive, require multiple steps, and involve bulky equipment. As an alternative, electrochemical sensors have gained attention for their simplicity, accuracy, speed, and selectivity.[12] For instance, Lu et al. reported the use of ceria nanocubes as a catalyst for a direct electrochemical sensor of bilirubin, which can selectively detect free bilirubin within a short response time.[13] However, enhancing the response sensitivity of bilirubin electrochemical sensors remains challenging due to the low free bilirubin content in serum.

As an emerging class of porous materials, metal–organic frameworks (MOFs), built from the assembly of metallic ions/clusters and organic ligands, boast high specific surface areas, clearly defined pore sizes, high porosity, and tailored chemical functionalities.[14,15] These benefits allow MOFs to excel in various fields such as chemical sensing, gas storage/separation, catalysis, and drug delivery.[16–18] Particularly, MOFs have been extensively used in detecting biological factors including glucose, lactic acid, dopamine, and urea.[19–21] Du et al. reported the sensitive detection of bilirubin by using the Uio-66 type MOF. However, its particulate state limits its use in devices, and the

Z. Lu, Z. Xiao, J. Wang, J. Huang, J. Cui, Y. Mei, G. Huang
Department of Materials Science & State Key Laboratory of Molecular Engineering of Polymers
Fudan University
Shanghai 200438, P. R. China
E-mail: gshuang@fudan.edu.cn
Z. Lu, J. Wang, J. Cui, Y. Mei, G. Huang
Yiwu Research Institute of Fudan University
Yiwu, Zhejiang 322000, P. R. China
Z. Lu, Z. Xiao, J. Wang, J. Huang, J. Cui, Y. Mei, G. Huang
International Institute for Intelligent Nanorobots and Nanosystems
Fudan University
Shanghai 200438, P. R. China
Z. Lu
Shanghai Center of Biomedicine Development
Zhangjiang Hi-Tech Park, Shanghai 201203, P. R. China
Z. Zhao
College of Biological Science and Medical Engineering
Donghua University
Shanghai 201620, P. R. China
E-mail: zhezhao@dhu.edu.cn

The ORCID identification number(s) for the author(s) of this article can be found under https://doi.org/10.1002/admt.202400344

DOI: 10.1002/admt.202400344

linear range of single-metal MOF is relatively narrow.[22] Compared to monometallic compounds, bimetallic MOFs (BMOFs) and their derived composite materials provide several benefits, encompassing enhanced conductivity, expanded active sites, elevated charge capacity, and tunable electrochemical activity.[23–25] Moreover, the assembly layout on the BMOFs sensing electrode remains a 1D or 2D structure, restraining their application in the detection of intricate biological targets.[26] Numerous studies have been conducted to enhance the electrode material structure and strengthen the adhesion between BMOFs and the electrode.[27–29] For instance, MXene, carbon nanotubes, and BMOFs were formed into 1D heterostructures by using a winding assembly technique.[30,31] It has been shown that 3D crosslinked networks created from 1D heterogeneous components offer a broad spectrum of heterogeneous interfaces, stacked pore structures, and impressive electrical conductivity.[32] Even though researchers have selected high surface area substrates as electrodes, mixing them with BMOFs to boost electrical conductivity, several issues, such as weak adhesion and nonuniform growth, still persist.[33,34] Atomic layer deposition (ALD) is a gas-phase film deposition technique capable of conformally depositing a dense film of highly controllable thickness due to its self-limiting and self-saturating properties.[35] In previous work, it was demonstrated that an effective approach for incorporating MOF films into intricate conductive substrates was achieved through the induction of oxide nanomembranes prepared via ALD.[36] However, the controlled synthesis of BMOF films on 3D complex conductive substrates remains a pressing issue.

Here, we propose a stepwise synthesis strategy, by using ALD technology to introduce a metal oxide nanomembrane to customize the growth of FeCo-BDC MOF-based flexible nanofibers with bio-sensing function. For FeCo-based bimetallic catalysts, it is believed that the involved Fe sites are the main catalytic active centers, while the Co species provide conductive networks and synergistic effects for the Fe sites. The bimetallic MOF nanomembranes synthesized through the induction effect of ALD oxide nanomembranes can grow densely and uniformly on the surface of 3D flexible fibers, which optimizes synthesized complex conductive nanofibers. We find that the corresponding electrode indeed shows excellent electrochemical sensing performance toward bilirubin. It presents a linear relationship in a low bilirubin concentration range of 2.5–50 μM with a sensitivity as high as 4067 μA mM^{-1} cm^{-2} and a detection limit as low as 0.36 μM. This is a significant improvement over previously reported MOF-based enzyme-free bilirubin sensors.

2. Results and Discussion

2.1. Assembly and Characterization of FeCo-BDC MOF@C-PAN Nanofibers

Figure 1a is a schematic demonstration of the present work, which shows that the ZnO nanomembrane supported on carbonized polyacrylonitrile (C-PAN) nanofibers are first prepared via ALD to assist the growth of subsequent BMOF film with solid adhesion. Then, the produced FeCo-BDC MOF@C-PAN nanofibers are applied to detect artificial urine via electrochemical signals. The structure of these compound nanofibers was inspected by using Scanning Electron Microscopy (SEM). Initially, ZnO nanomembranes were introduced onto carbonized nanofibers by ALD to facilitate the establishment of strongly adhered BMOF films. The solid adhesion between the ZnO nanomembrane and the foundational fibers contributes to substantial structural stability, optimizing the overall fabrication process, as depicted in Figure 1b,c. Moreover, via a hydrothermal method, the MOF film can be uniformly loaded onto the surface of the substrate, presenting conformal assembled nanosheets on the nanofibers (Figure 1d). The bimetallic FeCo-BDC MOF film presents a globular formation uniformly loaded onto the fiber. SEM images of Fe-BDC MOF@C-PAN nanofibers and Co-BDC MOF@C-PAN nanofibers are also shown in Figure S1 (Supporting Information) for comparison and different morphologies can be observed. Furthermore, the energy-dispersive X-ray spectroscopy (EDS) mapping of FeCo-BDC MOF@C-PAN nanofibers, seen in Figure 1e–j and Figure S2 (Supporting Information), indicates a uniform distribution of C, N, O, Fe, and Co elements within the nanofibers. According to our previous research, the growth mechanism and nucleation process of FeCo-BDC MOF films induced by ALD ZnO nanomembrane should be divided into several steps.[37] First, the ZnO nanomembrane reacts with $Co(NO_3)_2$ and $FeCl_3$ to generate (Zn, Fe) and (Zn, Co) hydroxyl double salts (HDS). Subsequently, when exposed to the organic linker (TPA), $COOH^-$ in the TPA provides reactive electrons to disrupt the crystal structure of HDS.[38] As HDS is gradually exposed to TPA, Fe^{3+} and Co^{2+} are successively attached to TPA. Eventually, HDS is transformed into FeCo-BDC and uniformly assembled on the fiber surface after the aging process. The whole induced assembly process may be described by the following two equations:

$$Co(NO_3)_2 \cdot 6H_2O + FeCl_3 + ZnO \rightarrow (Zn, Fe_2)(OH)_2Cl_6 + (Zn, Co)_2(OH)_3NO_3 \quad (1)$$

$$(Zn, Fe_2)(OH)_2Cl_6 + (Zn, Co)_2(OH)_3NO_3 + H_2BDC \rightarrow [FeCo - BDC]_n + Zn(NO_3)_2 \quad (2)$$

2.2. Structure Analyses

Fourier transform infrared (FTIR) spectroscopy was used to analyze the functional groups in Fe-BDC MOF@C-PAN nanofibers, Co-BDC MOF@C-PAN nanofibers, and FeCo-BDC MOF@C-PAN nanofibers (**Figure** 2a). The absorption peaks at 750 and 810 cm^{-1} are attributed to the bending vibration of the C—H bond in the benzene ring of the organic ligand.[39] The peak at 1384 cm^{-1} corresponds to a symmetrical vibration of —COOH, indicating the presence of H_2BDC as an organic ligand in the synthetic sample.[40] The tensile vibrations of C = C and C = O produce adsorption peaks at 1582 and 1620 cm^{-1}, respectively.[41] The low-frequency absorption peaks of less than 600 cm^{-1} are attributed to the vibrations of the metal-oxo (Co—O and Fe—O) bond.[42] Therefore, the signals observed at 456 and 526 cm^{-1} are assigned to the tensile vibrations of Co—O and Fe—O, respectively, demonstrating the successful fabrication of bimetallic

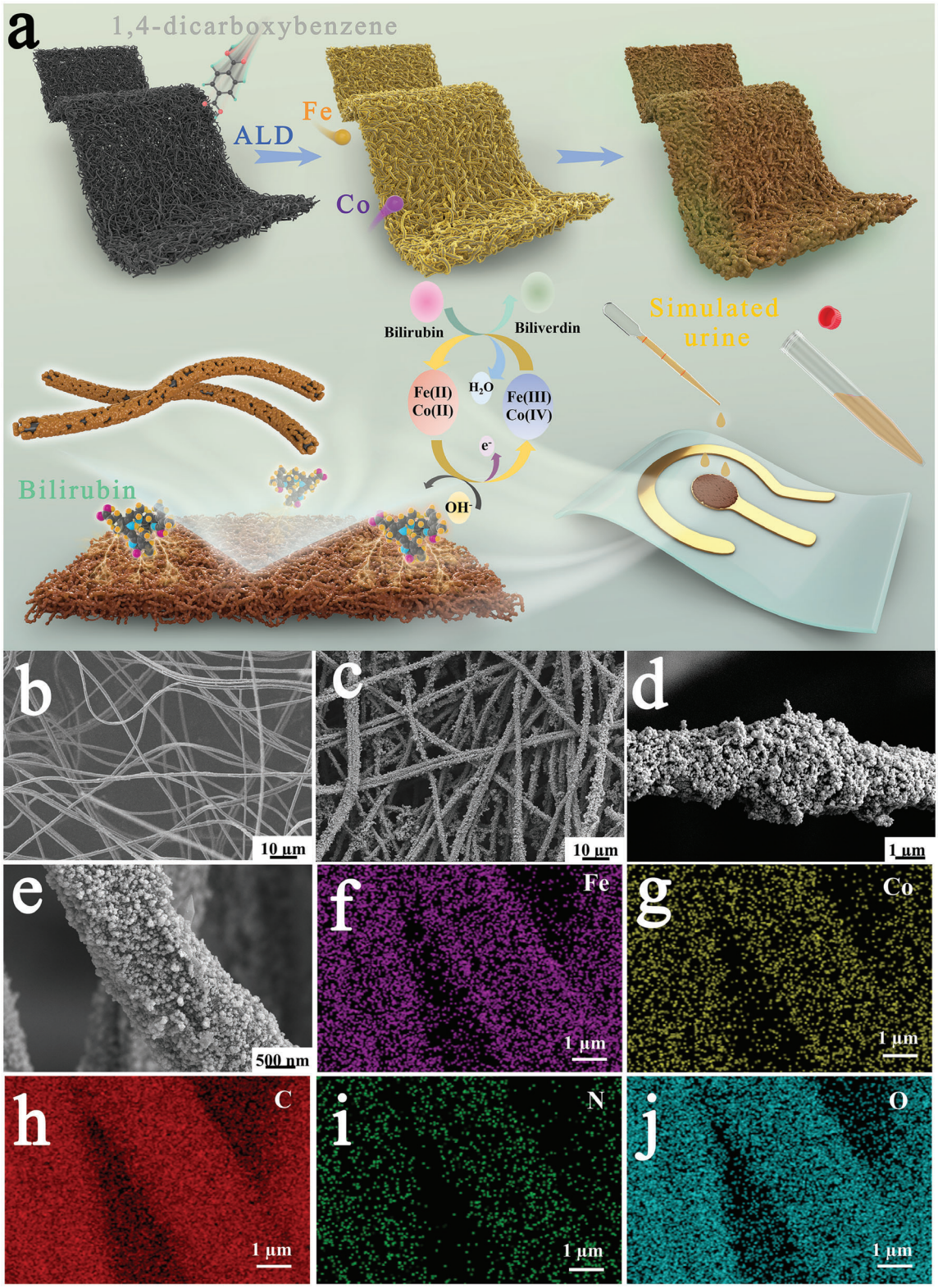

Figure 1. a) Illustration of the present work. The ZnO nanomembrane supported on carbonized C-PAN nanofibers is first prepared via ALD at 120 °C (the first step), and then the FeCo-BDC MOF grow onto the treated nanofibers via hydrothermal process (the second step). The device is prepared by using FeCo-BDC MOF@C-PAN nanofibers for bilirubin sensing. The sensing mechanism is also schematically demonstrated. b) SEM image of initial C-PAN nanofibers. c) SEM image of FeCo-BDC MOF@C-PAN nanofibers. d) High reselotion SEM image of FeCo-BDC MOF@C-PAN nanofibers. e–j) EDS mapping of FeCo-BDC MOF@C-PAN nanofibers.

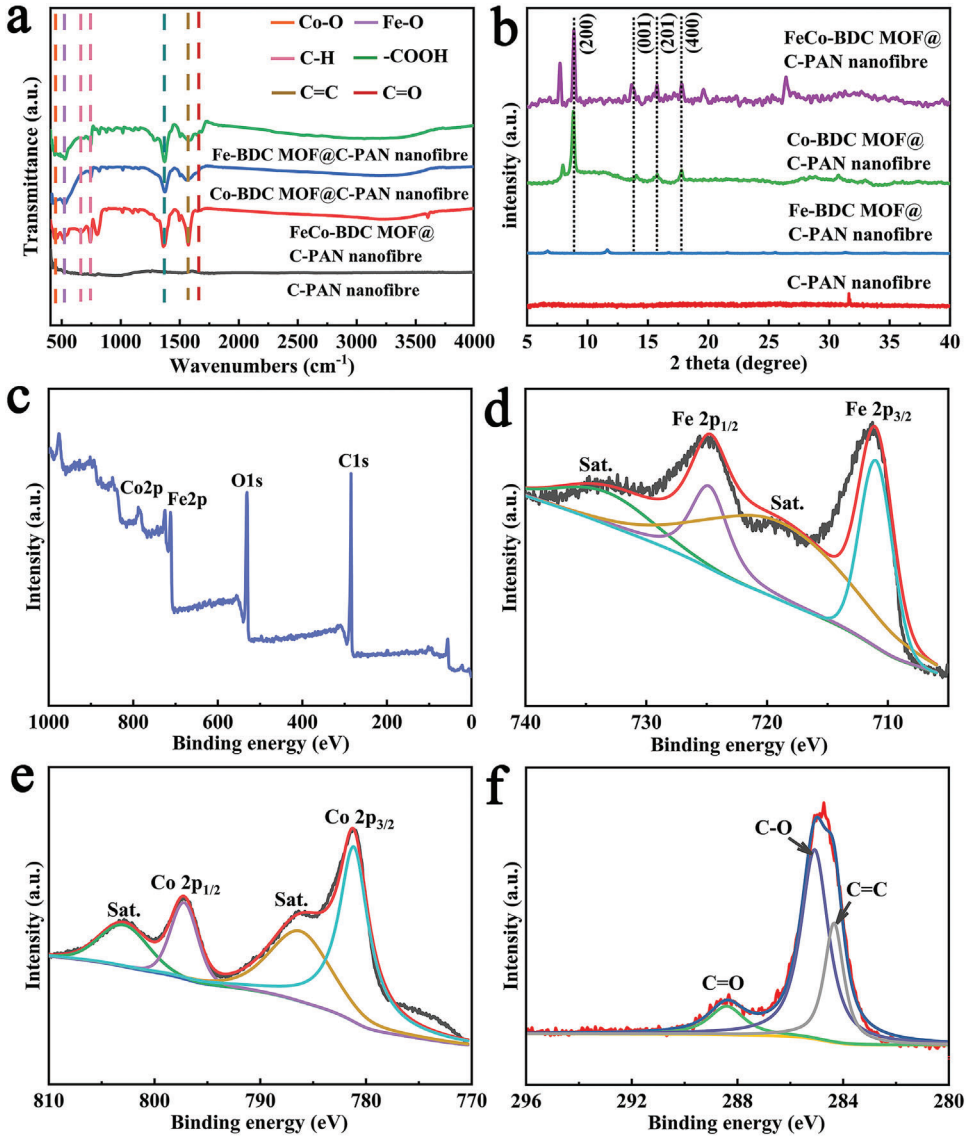

Figure 2. a) FTIR curves of C-PAN nanofibers, Fe-BDC MOF@C-PAN nanofibers, Co-BDC MOF@C-PAN nanofibers, and FeCo-BDC MOF@C-PAN nanofibers. b) XRD patterns of C-PAN nanofibers, Fe-BDC MOF@C-PAN nanofibers, Co-BDC MOF@C-PAN nanofibers, and FeCo-BDC MOF@C-PAN nanofibers. c) XPS spectrum of FeCo-BDC MOF@C-PAN nanofibers. d) High-resolution Fe 2p spectrum of FeCo-BDC MOF@C-PAN nanofibers. e) High-resolution Co 2p spectrum of FeCo-BDC MOF@C-PAN nanofibers. f) High-resolution C 1s spectrum of FeCo-BDC MOF@C-PAN nanofibers.

FeCo-BDC MOF-based film on the substrate. The crystal structures of the samples were analyzed by XRD (Figure 2b). The broad peak at 32° of C-PAN nanofibers was attributed to the amorphous structure of the carbon backbone. No obvious diffraction peak was detected in Fe-BDC MOF@C-PAN nanofibers, and the crystallinity was poor. In contrast, for Co-BDC@C-PAN nanofibers and FeCo-BDC@C-PAN nanofibers, several diffraction peaks were observed at 8.8°, 13.7°, 15.7°, and 17.7°, which could be assigned to the (200), (001), (201), and (400) planes of the layered trinity structure, respectively,[43] and FeCo-BDC@C-PAN nanofibers have stronger diffraction intensity. These observations suggest that FeCo-BDC MOF@C-PAN nanofibers may have a similar layered ternary structure to Co-BDC MOF@C-PAN nanofibers,[44] but the crystallinity is further enhanced by the introduction of secondary metal ions. X-ray photoelectron spectroscopy (XPS) further demonstrated the presence of Fe, Co, C, and O elements in FeCo-BDC MOF@C-PAN nanofibers (Figure 2c). As shown in Figure 2d, the Fe 2p spectrum consists of four peaks and one satellite peak. In the spin orbits of Fe $2p_{3/2}$ and Fe $2p_{1/2}$, the binding energies of 711.0 and 724.2 eV correspond to Fe^{2+},[45] while the binding energies of 713.4 and 725.1 eV correspond to Fe^{3+}.[46] Meanwhile, four peaks and two satellite peaks were observed in the Co 2p spectrum. The Co $2p_{3/2}$ region can be divided into Co^{3+} (781.3 eV) and Co^{2+} (783.2 eV), and the Co $2p_{1/2}$ region can be divided into Co^{3+} (797.13 eV) and Co^{2+} (798.5 eV), respectively.[43] The two oxidation states of

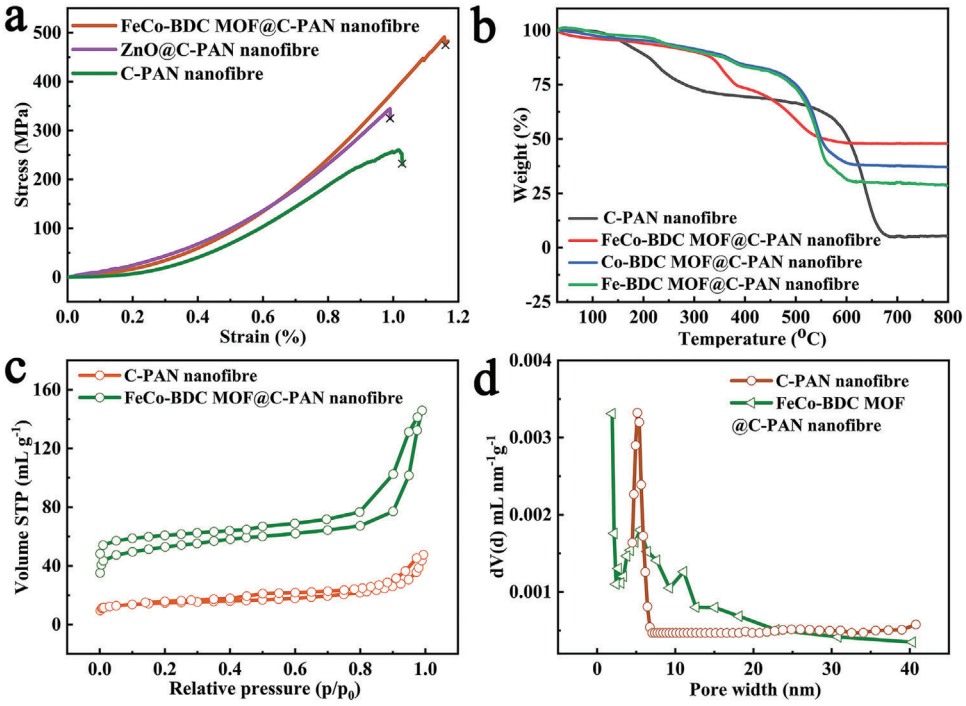

Figure 3. a) Strain and stress curves of C-PAN nanofibers, ZnO@C-PAN nanofibers, and FeCo-BDC MOF@C-PAN nanofibers. b) TGA curves of the prepared samples. c) N_2 adsorption–desorption isotherms of C-PAN nanofibers and FeCo-BDC MOF@C-PAN nanofibers. d) Pore size distribution of corresponding nanofibers.

Fe and Co might originate from the fact that the growth process of MOF undergoes HDS transformation, and the residual HDS contains Co^{2+} and Fe^{3+}. Additionally, the presence of C = O (288.4 eV), C—O (285.0 eV), and C = C (284.3 eV) species in the C1s spectrum (Figure 2f) can be identified.[47] These results are consistent with the FTIR results. Therefore, the above characteristics confirm the successful fabrication of Fe-BDC MOF@C-PAN nanofibers, Co-BDC MOF@C-PAN nanofibers, and FeCo-BDC MOF@C-PAN nanofibers.

Tensile measurement was used to investigate the mechanical properties of composite nanofibers as shown in **Figure 3a**. The results showed that the original carbon nanofibers possess certain tensile properties, but the tensile performance was enhanced to a certain extent after loading with ZnO nanomembranes and subsequent hydrothermal reactions. This phenomenon is mainly attributed to the metal oxide layer increasing the bonding strength between the MOF thin film and the substrate fibers, and the connections between MOF particles concurrently enhancing the mechanical properties of the composite nanofibers. The thermal stability of the prepared MOF-based composite nanofibers was investigated by thermogravimetric analysis (TGA) (Figure 3b). It can be seen that at temperatures greater than 600 °C, the weight is greatly reduced, which may be attributed to the oxidative degradation of the organic linker. It also demonstrated that the composite nanofibers have excellent structural stability and are suitable for a wide temperature range. In addition, the results show that the FeCo-BDC MOF@C-PAN nanofibers can maintain good thermal stability, which is conducive to subsequent electrochemical detection. The Brunauer–Emmett–Teller (BET) surface area and corresponding pore distribution of the samples were obtained, as shown in Figure 3c,d. It can be seen that FeCo-BDC MOF@C-PAN nanofibers exhibit type I and IV isotherms, indicating the coexistence of micropores and mesopores in FeCo-BDC MOF@C-PAN nanofibers. The pore size distribution shows a micropore peak at 1.9 nm, and mesoporous peaks at ≈5 and 10 nm are also evident. According to our previous research, microporosity is mainly attributed to the porosity of MOFs, and mesoporosity is from stacked MOF particles on the fiber surface. In addition, the adsorption and desorption isotherms also show that the specific surface area of the FeCo-BDC MOF@C-PAN nanofibers is 150 m^2g^{-1}.

2.3. Electrochemical Evaluation

The fabricated FeCo-BDC MOF@C-PAN nanofibers are used for bilirubin sensing. The electrochemical properties of FeCo-BDC MOF@C-PAN nanofibers are specifically investigated by cyclic voltammetry (CV) in 0.1 M NaOH solution at a scan rate of 60 mV s^{-1} in the potential range of —0.3 to 0.6 V. As depicted in Figure S3 (Supporting Information), the oxidation peak at ≈0.3 V and the reduction peak at ≈0.1 V are associated with the oxidation and reduction processes of the composites, respectively. It is noteworthy that in electrolytes containing 50 µM bilirubin, the current responses of the reduction peak and oxidation peak significantly enhanced, indicating that the composite can generate additional current through catalyzing the oxidation of bilirubin. As schematically illustrated in Figure 1a, the

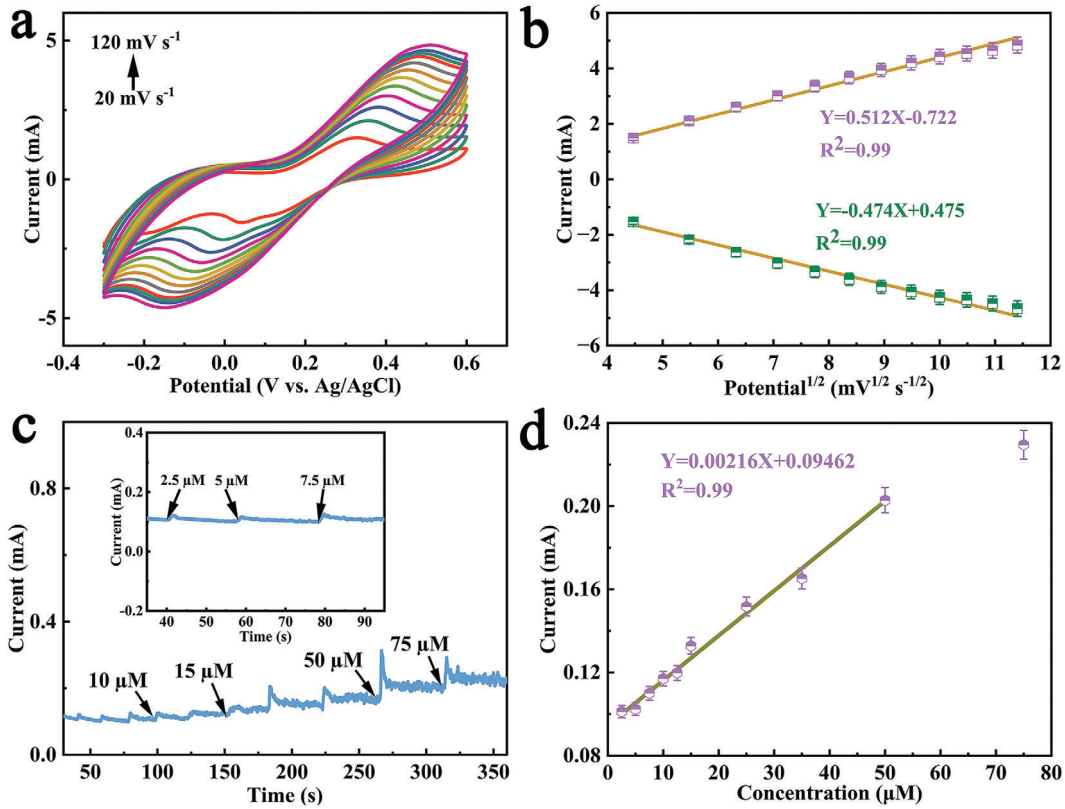

Figure 4. a) CV scans of FeCo-BDC MOF@C-PAN nanofibers were conducted at varying scan rates, ranging from 20 to 120 mV s^{-1}, in 0.1 M NaOH solution containing 5 mM $K_3[Fe(CN)_6]$. b) Calibration plot corresponding to (a). c) Amperometry measurements for FeCo-BDC MOF@C-PAN nanofibers. The measurement was taken with the progressive addition of bilirubin at various concentrations into 0.1 M NaOH electrolyte at a voltage of 0.6 V. Inset is the electrochemical response curve of bilirubin at low concentrations. d) Calibration plot derived from (c).

mechanism of bilirubin sensing can be described by the following equations:[13,37]

$$[\text{Fe (II) Co (II) (BDC)}_2]_n + 2nOH^- \rightarrow [\text{Fe (III) Co (III) (BDC)}_2\text{ (OH) }]_n + 2ne^- \quad (3)$$

$$[\text{Fe (III) Co (III) (BDC)}_2\text{ (OH) }]_n + nOH^- \rightarrow [\text{Fe (III) Co (IV) (BDC)}_2\text{ (OH) }]_n + ne^- \quad (4)$$

$$2\left[\text{Fe (III) Co (IV) (BDC)}_2\text{ (OH)}\right]_n + nC_{33}H_{36}N_4O_6 \rightarrow 2\left[\text{Fe (II) Co (II) (BDC)}_2\right]_n + nC_{33}H_{34}O_6N_4 + 2nH_2O \quad (5)$$

During the process, Co^{2+} is oxidized sequentially to Co^{3+} and Co^{4+} in an alkaline aqueous solution and the oxidation of bilirubin to biliverdin is related to the reduction process of Fe^{3+} and Co^{4+}. In our previous work, theoretical calculations confirmed that multifunctional oxidation states of metal ions in the MOF would facilitate electrochemical reactions more easily and more reactively.[48] We also performed a control experiment to detect bilirubin by using Cu-BDC MOF with a single oxidation state, and the results in Figure S4 (Supporting Information) demonstrate low sensitivity and a large detection limit. Furthermore, the surface active area of the FeCo-BDC MOF@C-PAN nanofibers was analyzed by $K_3[Fe(CN)_6]$ probe. **Figure 4a** shows the CV results of the FeCo-BDC MOF@C-PAN nanofibers, with a set of oxidation and reduction peaks observed at different CV scan rates, and the response currents of these peaks increase as the scan rate increases from 20 to 120 mV s^{-1}. In this work, the effective area of the detection electrode is calculated according to the Randles-Sevcik formula:[49]

$$I_{peak} = (2.69 \times 10^5)n^{3/2}SD^{1/2}Cv^{1/2} \quad (6)$$

where n is the amount of transfer electrons, and D and C are the diffusion coefficient and volume concentration of $K_3[Fe(CN)_6]$, respectively. According to this formula and the calibration line of Figure 4b, the effective active area is determined to be 0.15 cm^{-2}, which is conducive to the contact of active species in the electrolyte and the transfer of interfacial electrons, reflecting the electrochemical property. As described in Figure S5 (Supporting Information), the S values of Fe-BDC MOF@C-PAN nanofibers and Co-BDC MOF@C-PAN nanofibers are merely 0.054 and 0.050 cm^{-2}, respectively. The synergistic effect of bimetallic MOF significantly enhances the actual active area of the electrode.

The bilirubin detection performance of the composite was specifically evaluated. First, the sensing performance of the composite nanofibers was studied by current-time (*I-t*) curves. Figure S6 (Supporting Information) shows the effect of the applied

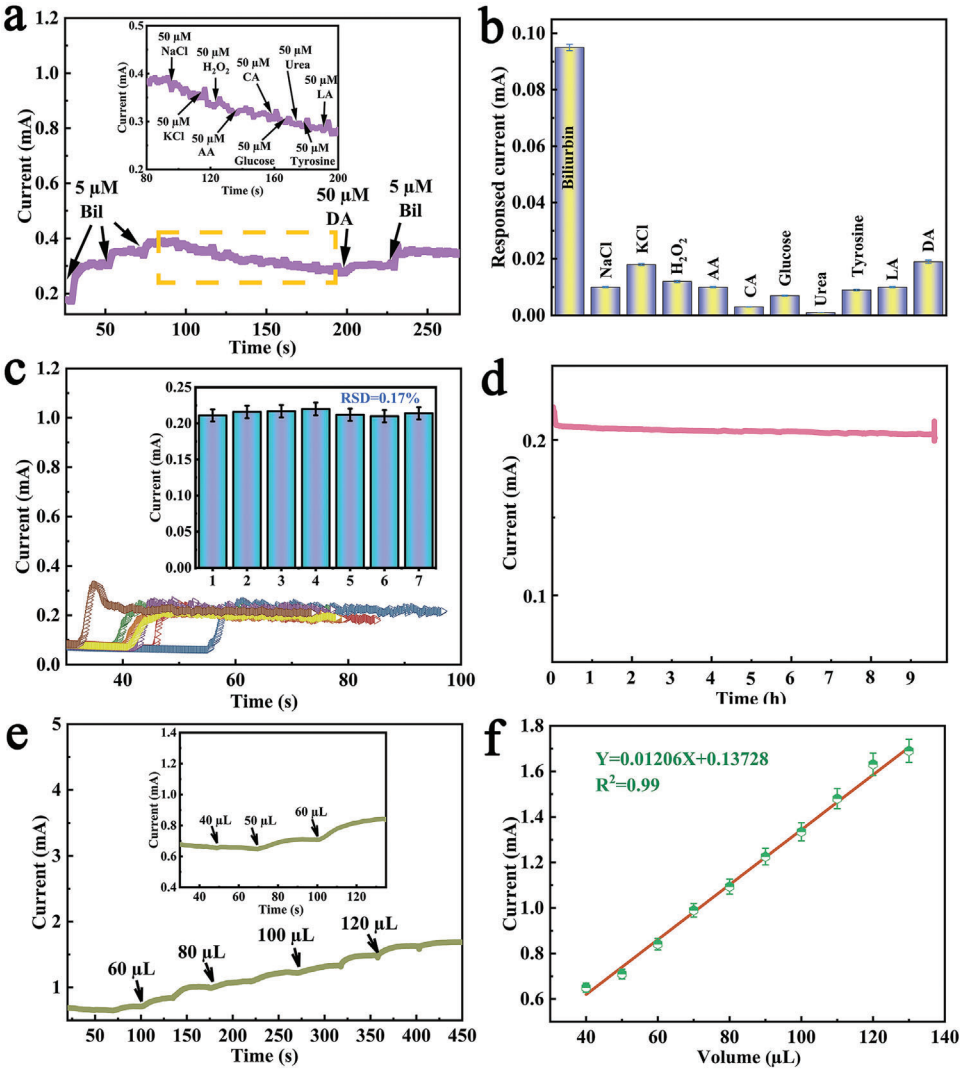

Figure 5. a) Amperometry measurements have been undertaken on FeCo-BDC MOF@C-PAN nanofibers, with bilirubin (Bil) and other interfering substances progressively added. The inset is the enlarged plot. b) Current responses are measured at 0.6 V for 50 μM different substances including Bil, NaCl, KCl, H_2O_2, AA, CA, glucose, urea, tyrosine, LA, and DA. c) *I-t* curves of the FeCo-BDC MOF@C-PAN nanofibers when 1 mM biliurbin is added seven times. The inset is the statistics of corresponding current responses. d) *I-t* curve of FeCo-BDC MOF@C-PAN nanofibers in 0.1 M NaOH solution with 50 μM biliurbin at 0.6 V. 50 μM biliurbin was dropped to the solution after 8 h to measure the recovery performance. e) I-t curve of FeCo-BDC MOF@C-PAN nanofibers in simulated urine containing bilirubin. The inset is the enlarged plot. f) Calibration plot derived from (e).

potential on the current response. It is evident that our composite nanofibers exhibit a significant and stable current response at 0.6 V. Therefore, detailed *I-t* tests of the FeCo-BDC MOF@C-PAN nanofibers electrode were performed at 0.6 V. Figure 4c shows the *I-t* recordings of the composite sensor when bilirubin is continuously added to 0.1 M NaOH electrolyte. The results show that the composite nanofibers have an obvious fast current response and real-time bilirubin detection ability. The corresponding calibration curves for bilirubin detection by the FeCo-BDC MOF@C-PAN nanofibers are shown in Figure 4d, according to which the composites have a high sensitivity of 4067 μA mM^{-1} $cm^{-2}$and a linear relationship at low concentrations of 2.5–50 μM. Additionally, according to the equation: limit of detection (LOD) = $3\delta/S$, where δ is a standard deviation and S is sensor sensitivity, LOD could be as low as 0.36 μM for the FeCo-BDC MOF@C-PAN nanofibers based sensor. Table S1 (Supporting Information) presents a detailed comparison of the performance of current nanofiber sensors and those reported in the literature. The outstanding sensing performance could be attributed to the following fundamental factors. First, as previously described, the oxide nanomembrane induces the assembly of BMOF film, resulting in strong adhesion and uniform coatings, and BMOF particles are tightly stacked to form dense functional films. This could greatly improve structural stability. Second, multiple conductive pathways in the 3D conductive substrate promote electron transfer and further improve the sensing performance.

Interference immunity is also an important factor in the practical use of bilirubin sensors. The *I-t* curve of FeCo-BDC MOF@C-PAN nanofibers is shown in **Figure** 5a,b with the continuous addition of 5 μM bilirubin, 50 μM NaCl, 50 μM KCl, 50 μM H_2O_2,

50 μM ascorbic acid (AA), 50 μM CA, 50 μM glucose, 50 μM urea, 50 μM tyrosine, 50 μM lactate (LA), and 50 μM dopamine (DA). It can be seen that the current response of the target factor, bilirubin, is evident. However, for the addition of interference sources, only negligible responses can be observed. In addition, when three times the number of interference sources is added, the current has a weak response, but it is also negligible, as shown in Figure S7 (Supporting Information). These results show that the prepared FeCo-BDC MOF@C-PAN has good selectivity and anti-interference properties. Additionally, the sensor device's reproducibility in detecting bilirubin is very important. Figure 5c and its inset respectively show the response current curves and the response current values for seven repeated tests for 50 μM bilirubin at 0.6 V. The results prove that the composite nanofibers maintained good reproducibility. The inset shows that the relative standard deviation is as low as 0.17%. Meanwhile, the composite exhibits a stable current response at ≈0.18 mA for 9 h (Figure 5d). In addition, the XPS results further confirmed that the active layer (i.e., FeCo-BDC MOF film) can be firmly attached to the substrate with the help of ALD induction (Figure S8, Supporting Information). The SEM images provide further details after 9 h of *I-t* measurement, where no significant morphological alteration can be spotted. Moreover, there is no evidence of the peeling off of BMOF film. The results all confirm the effective attachment of the active layer to the substrate, a result achieved with the aid of ALD induction (Figures S9 and S10, Supporting Information).

To further assess the detection feasibility of the fabricated FeCo-BDC MOF@C-PAN nanofibers electrochemical sensor, the determination of free bilirubin in the urine sample was performed. We prepared a device for detecting bilirubin in artificial urine. In the experiment, an amount of bilirubin was added to artificial urine to simulate the urine of jaundice patients. Figure 5e shows the I-t curve of the device testing the urine sample and the corresponding calibration plot is shown in Figure 5f. It can be seen that the current response increases with the amount of added urine. Meanwhile, in order to eliminate the interference from other biological factors in the urine, we also tested the initial urine without adding bilirubin and found that no current response was obtained (Figure S11, Supporting Information). In addition, the recovery results are presented in Table S2 (Supporting Information). The FeCo-BDC MOF@C-PAN nanofibers sensor exhibits an impressive recovery rate, ranging from 95.2% to 96.7%. The results indicate the feasibility for the determination of free bilirubin in urine samples.

3. Conclusion

In summary, we propose an enzyme-free and non-invasive biosensor based on flexible fiber and bimetallic MOF film for highly sensitive real-time detection of bilirubin. Through the combination of ALD and hydrothermal synthesis, we synthesized FeCo-BDC MOF@C-PAN nanofibers, which serve as an effective active material for the detection of bilirubin. Owing to the hierarchical structure of the bimetallic MOF film and the interconnected conductive network of the high-conductivity substrate, FeCo-BDC MOF@C-PAN nanofibers exhibit excellent sensing performance for bilirubin with a high sensitivity (4067 $\mu A\ mM^{-1}\ cm^{-2}$) and a low detection limit (0.36 μM). Meanwhile, the device exhibits excellent analyte recognition ability and stability. The detection of bilirubin in actual urine verified that the sensor possesses practical detection feasibility. However, at present, sensor detection employs an electrochemical workstation, making it challenging to implement portable devices for daily real-time monitoring of jaundiced patients, which needs further research effort to produce an integrated and portable characterization setup. Nevertheless, we believe that achieving the controlled synthesis of bimetallic MOF films on flexible fibers suggests new application potential for rapid and non-invasive sensitive detection of bilirubin on future wearable devices, and this is also our future research objective.

4. Experimental Section

Materials: All chemical materials and reagents were received from commercial supplies and used as obtained. Ferric chloride ($FeCl_3$, AR, 99%), cobaltous nitrate hexahydrate ($Co(NO_3)_2{\cdot}6H_2O$, AR, 99%), polyvinyl pyrrolidone (PVP, Mw = 1300), polyacrylonitrile (PAN, Mw = 13 000), terephthalic acid (TPA, AR, 99%), sodium hydroxide (NaOH, AR, 97%), and *N,N*-Dimethylformamide (DMF, AR, 95%) were purchased from Aladdin (Shanghai, China). Bilirubin (Bil, AR, 99%), NaCl (AR, 99%), KCl (AR, 99%), ascorbic acid (AA, AR, 99%), L-Ascorbic acid (ASA, AR, 99%), urea (AR, 99%), dopamine (DA, AR, 99%), and lactic acid (LA, AR, 99%) were purchased from Sinopharm Chemical Reagent Co., Ltd. Potassium ferricyanide ($K_3[Fe(CN)_6]$, AR, 99%) was purchased from Aladdin (Shanghai, China). Artificial urine was purchased from Xinheng Company. Deionized (DI) water was received from Millipore, Direct-Q5.

Preparation of C-PAN Nanofibers: The 1 g of PTA was first dissolved in 18 g of DMF at 50 °C for 30 min, and then 2 g of PAN and 1 g of PVP were mixed with the above TPA/DMF solution for 24 h under magnetic stirring. The resulting mixed spinning paint was loaded into a 20 mL syringe with a 19-gauge needle and electrospun at a flow rate of 3 mL h^{-1} at 20 kV. The rotational speed of the roller collector and the distance from the needle to the roller collector are fixed at 60 RPM and 20 cm, respectively. Maintaining a high humidity level is essential for the production of precursor fibers, for which a humidifier (Levoit) is used to regulate the humidity in the electrospinning chamber, which is controlled at 70–80%. The sample was kept at a final temperature for 2 h by heating to 260 °C at a rate of 3 °C min^{-1} for 1 h and then carbonized to 1100 °C at a heating rate of 5 °C min^{-1} under an argon gas stream (≈99% purity).

Preparation of Fe-BDC MOF@C-PAN Nanofibers: First, the C-PAN nanofibers were acid-washed and dried, then a 300 nm ZnO layer was loaded onto the fiber surface at 120 °C by using ALD (sample name: ZnO@C-PAN nanofibers). A precursor solution (solution A) was prepared by dissolving 2 mmol of $FeCl_3$ in 20 mL of DMF and ZnO@C-PAN nanofibers were immersed into solution A. The mixture was then placed in an oven at 150 °C for 24 h. After that, the mixture was cooled down to room temperature. A 2 mmol TPA solution (solution B) was prepared by dissolving it in 20 mL of DMF, and then Solution B was slowly added to solution A. The mixture was then returned to the oven at 150 °C for another 24 h. The resulting composite fibers were washed three times in deionized water using ultrasonic treatment and then dried at 60 °C for 24 h.

Preparation of Co-BDC MOF@C-PAN Nanofibers: A precursor solution (Solution C) was prepared by dissolving 2 mmol of $Co(NO_3)_2{\cdot}6H_2O$ in 20 mL of DMF and ZnO@C-PAN nanofibers were immersed into solution A. The mixture was then placed in an oven at 150 °C for 24 h. After that, the mixture was cooled down to room temperature. Then solution B was slowly added to solution C. The mixture was then returned to the oven at 150 °C for another 24 h. The resulting composite fibers were washed three times in deionized water using ultrasonic treatment and then dried at 60 °C for 24 h.

Preparation of FeCo-BDC MOF@C-PAN Nanofibers: A 2 mmol $FeCl_3$ and 2 mmol $Co(NO_3)_2{\cdot}6H_2O$ solution was then prepared in 20 mL of DMF to create precursor solution D, and the ZnO@C-PAN nanofibers were immersed into this solution. The mixture was then placed in an oven at 150 °C

for 24 h. After that, the mixture was cooled to room temperature. Then solution B was slowly added to solution D. The combined mixture was once again placed in the oven at 150 °C for another 24 h. The resulting composite material was cleaned three times with deionized water using an ultrasonic treatment and then dried at 60 °C for 24 h.

Preparation of Cu-BDC MOF@C-PAN Nanofibers: A precursor solution (Solution E) was prepared by dissolving 2 mmol of $Cu(NO_3)_2{\cdot}3H_2O$ in 20 mL of DMF and ZnO@C-PAN nanofibers were immersed into solution E. The mixture was then placed in an oven at 150 °C for 24 h. After that, the mixture was cooled down to room temperature. Then solution B was slowly added to solution E. The mixture was then returned to the oven at 150 °C for another 24 h. The resulting composite fibers were washed three times in deionized water using ultrasonic treatment and then dried at 60 °C for 24 h.

Microstructural Characterizations: Microstructural characterizations were performed by using various methods. SEM images were acquired with Zeiss Sigma 300 SEM. EDS mapping was conducted via a Zeiss Ultra 55 SEM at 20 kV. XRD spectra were collected using a Thermo Fisher ARL EQUINOX 3000 device. XPS data were gathered using an ESCALAB QXi XPS. BET analysis at 77 K was performed using a Micromeritics ASAP2420 instrument, with all results derived after a pretreatment at 120 °C dynamic vacuum for 12 h. FTIR was carried out with a Thermo Nicolet IS5 device at room temperature. TGA was conducted using an STA8000 instrument with a heating rate of 10 °C min^{-1} under an air atmosphere.

Electrochemical Measurements: All electrochemical experiments were conducted at room temperature using a three-electrode system with an electrochemical workstation (Chenhua CHI-760E). A carbon rod and an Ag/AgCl electrode (1.0 M KCl, 25 °C) were utilized as the counter electrode and reference electrode, respectively. The samples were cut into pieces (0.5 × 1.0 cm^2) and subsequently attached to the platinum electrode clamp.

Supporting Information

Supporting Information is available from the Wiley Online Library or from the author.

Acknowledgements

Z.H.L., Z.J.X., and J.L.W. contributed equally to this work. This work was supported by the National Key Technologies R&D Program of China (No. 2021YFA0715302), the National Natural Science Foundation of China (No. 52203328), the Science and Technology Commission of Shanghai Municipality (Nos. 22ZR1405000 and 21ZR1403500).

Conflict of Interest

The authors declare no conflict of interest.

Data Availability Statement

The data that support the findings of this study are available from the corresponding author upon reasonable request.

Keywords

composite nanofiber, FeCo-BDC MOFs, flexible fibrous device, noninvasive bilirubin sensor

Received: February 29, 2024
Revised: May 24, 2024
Published online: June 11, 2024

[1] Y. Du, X. Li, X. Lv, Q. Jia, *ACS Appl. Mater. Interfaces.* **2017**, *9*, 30925.
[2] Q. Li, W. Zhao, H. Guo, J. Yang, J. Zhang, M. Liu, T. Xu, Y. Chen, L. Zhang, *ACS Appl. Mater. Interfaces.* **2020**, *12*, 25546.
[3] K. Yamazaki, K. Shinke, T. Ogino, *Coll. Surf., B* **2013**, *112*, 103.
[4] N. Cai, Q. Li, J. Zhang, T. Xu, W. Zhao, J. Yang, L. Zhang, *Coll. Interface Sci.* **2017**, *503*, 168.
[5] J. Chen, G. Song, Y. He, Q. Yan, *Microchim. Acta.* **2007**, *159*, 79.
[6] C. Berde, B. Hudson, R. Simoni, L. Sklar, *J. Biol. Chem.* **1979**, *254*, 391.
[7] S. Sahoo, S. Hsu, D. Chou, G. Wang, C. Chang, *Biosens. Bioelectron.* **2022**, *213*, 114440.
[8] H. Noh, M. Won, Y. Shim, *Biosens. Bioelectron.* **2014**, *61*, 554.
[9] J. Bell, M. Mousavi, M. Rahman, E. Tan, S. Vanniasinkam, G. Whitesides, *Biosens. Bioelectron.* **2019**, *126*, 115.
[10] K. P. M. Heiwegh, J. Fevery, N. Blackaert, *Chromatogr., Biomed. Appl.* **1989**, *496*, 1.
[11] M. Santhosh, S. Chinnadayyala, A. Kakoti, P. Goswami, *Biosens. Bioelectron.* **2014**, *59*, 370.
[12] A. S. G. Manoj, *Polym. Adv. Technol.* **2024**, *35*, e6346.
[13] Z. J. Lu, Y. R. Cheng, Y. Zhang, X. F. Wang, P. C. Xu, H. T. Yu, X. X. Li, *Sensor Actuat. B-Chem.* **2021**, *329*, 129224.
[14] A. Vignesh, P. Vajeeston, M. Pannipara, A. G. Al-Sehemi, Y. Xia, G. G. Kumar, *Chem. Eng. J.* **2022**, *430*, 133157.
[15] Z. Zhao, Y. Kong, G. Huang, C. Liu, C. You, Z. Xiao, H. Zhu, J. Tan, B. Xu, J. Cui, X. Liu, Y. Mei, *Nano Today* **2022**, *42*, 101347.
[16] M. M. Ahmad, M. Roushani, S. Farokhi, *Microchem. J.* **2024**, *197*, 109737.
[17] M. Roushani, Z. Saedi, T. M. Beygi, *J. Taiwan Inst. Chem. Eng.* **2016**, *66*, 164.
[18] J. Zhang, L. Liu, C. Zheng, W. Li, C. Wang, T. Wang, *Nat. Commun.* **2023**, *14*, 4922.
[19] M. Pappathi, P. Vajeeston, A. S. S. Raja, A. Vignesh, A. Syed, A. H. Bahkali, L. Cathrine, J. A. Sekar, A. Roveena, S. M. Phang, G. G. Kumar, *ACS Appl. Nano Mater.* **2023**, *6*, 14628.
[20] Z. Wang, Y. Huang, K. Xu, Y. Zhong, C. He, L. Jiang, J. Sun, Z. Rao, J. Zhu, J. Huang, F. Xiao, H. Liu, B. Xia, *Nat. Commun.* **2023**, *14*, 69.
[21] K. Ge, S. Sun, Y. Zhao, K. Yang, S. Wang, Z. Zhang, J. Cao, Y. Yang, Y. Zhang, M. Pan, L. Zhu, *Angew. Chem. Int. Ed.* **2021**, *60*, 12097.
[22] Y. R. Du, X. Q. Li, X. J. Lv, Q. Jia, *ACS Appl. Mater. Interfaces* **2017**, *9*, 30925.
[23] V. Archana, Y. Xia, R. Y. Fang, G. G. Kumar, *ACS Sustainable Chem. Eng.* **2019**, *7*, 6707.
[24] Z. M. Karazan, M. Roushani, *Electrocatalysis* **2024**, *15*, 110.
[25] M. Sarabaegi, M. Roushani, H. Hosseini, Z. Saedi, E. G. Lemraski, *Mater. Sci. Semicond. Process.* **2022**, *139*, 106351.
[26] X. Jiang, C. Shi, Z. Wang, L. Huang, L. Chi, *Adv. Mater.* **2024**, *36*, 2308952.
[27] N. Senthilkumar, G. G. Kumar, A. Manthiram, *Adv. Energy. Mater.* **2018**, *8*, 1702207.
[28] M. Y. Oh, J. J. Lee, A. Zahoor, G. G. Kumar, K. S. Nahm, *RSC Adv.* **2016**, *6*, 32212.
[29] T. R. Kumar, G. G. Kumar, A. Manthiram, *Adv. Energy. Mater.* **2019**, *9*, 1803238.
[30] C. Liu, Y. Bai, W. Li, F. Yang, G. Zhang, H. Pang, *Angew. Chem., Int. Ed.* **2022**, *61*, 202116282.
[31] Y. Shang, G. Xing, H. Lin, S. Chen, T. Xie, J. Lin, *Anal. Cham.* **2023**, *95*, 13368.
[32] J. Yang, Y. Ying, *Small* **2020**, *16*, 1906846.
[33] X. Yang, P. Qiu, J. Yang, Y. Fan, L. Wang, W. Jiang, X. Cheng, Y. Deng, W. Luo, *Small* **2021**, *17*, 1904022.
[34] D. Chronopoulos, H. Saini, I. Tantis, R. Zbořil, K. Jayaramulu, M. Otyepka, *Small* **2022**, *18*, 2104628.

[35] H. Li, Q. Lu, J. Shi, X. Zhang, P. Sun, X. Yan, G. Lu, *Adv. Funct. Mater.* **2024**, *34*, 2309383.
[36] Q. Zhang, L. Guo, H. Li, J. Huang, Z. Li, W. Hong, *Biotechnol. Appl. Biochem.* **2023**, *70*, 1024.
[37] Z. Zhao, Y. Kong, X. Y. Lin, C. Liu, J. R. Liu, Y. Y. He, L. L. Yang, G. S. Huang, Y. F. Mei, *J. Mater. Chem. A* **2020**, *8*, 26119.
[38] C. C. Ma, G. S. Gao, H. O. Liu, Y. Liu, X. F. Zhang, *J. Membr. Sci.* **2022**, *644*, 120167.
[39] H. H. Liu, G. Y. Li, C. W. Hu, *J. Mol. Catal. A: Chem.* **2013**, *377*, 143.
[40] H. X. Tong, Y. Ji, T. H. He, R. D. He, M. L. Chen, J. L. Zeng, D. X. Wu, *Water Sci. Technol.* **2022**, *86*, 95.
[41] H. Alamgholiloo, N. N. Pesyan, R. Mohammadi, S. Rostamnia, M. Shokouhimehr, *J. Environ. Chem. Eng.* **2021**, *9*, 105486.
[42] G. G. Kumar, K. Reddy, K. S. Nahm, N. Angulakshmi, A. M. Stephan, *J. Phys. Chem. Solids* **2012**, *73*, 1187.
[43] C. Yuan, J. Li, L. Hou, L. Yang, L. Shen, X. Zhan, *J. Mater. Chem.* **2012**, *22*, 16084.
[44] S. Mutahir, C. X. Wang, J. J. Song, L. Wang, W. Lei, X. Y. Jiao, M. A. Khan, B. J. Zhou, Q. Zhong, Q. L. Hao, *Appl. Mater. Today* **2020**, *21*, 100813.
[45] B. Iqbal, M. Saleem, S. N. Arshad, J. Rashid, N. Hussain, M. Zaheer, *Chem. - Eur. J.* **2019**, *25*, 10490.
[46] M. Wang, L. Yang, C. Guo, X. Liu, L. He, Y. Song, S. Fang, *ChemistrySelect* **2018**, *3*, 3664.
[47] S. K. Shaw, S. K. Alla, S. S. Meena, R. K. Mandal, N. K. Prasad, *J. Magnetism Magn. Mat.* **2017**, *434*, 181.
[48] Z. H. Lu, X. Y. Ke, Z. Zhao, J. Y. Huang, C. Liu, J. L. Wang, R. Y. Xu, Y. F. Mei, G. S. Huang, *ACS Appl. Mater. Interfaces* **2024**, *16*, 14218.
[49] X. Ke, Z. Zhao, J. Huang, C. Liu, G. Huang, J. Tan, H. Zhu, Z. Xiao, X. Liu, Y. Mei, J. Chu, *ACS Appl. Mater. Inter* **2023**, *15*, 12005.